Selectivity of Mo-NC sites for electrocatalytic N₂ reduction : a function of the single atom position on the surface and local carbon topologies

Selectivity of Mo-N-C sites for electrocatalytic N_2 reduction: A function of the single atom position on the surface and local carbon topologies

Parisa Nematollahi[*]

[*]Research Group Plasmant, NANOlab Center of Excellence, Department of Chemistry, University of Antwerp, Universiteitsplein 1, 2610 Antwerp, Belgium

* Corresponding author. **Phone:** (+32) 32652346. **E-mail**: parisa.nematollahi@uantwerpen.be

Abstract

Transition metal (TM) doped two-dimensional single-atom catalysts are known as a promising class of catalysts for electrocatalytic gas conversion. However, the detailed mechanisms that occur at the surface of these catalysts are still unknown. In the present work, we simulate three Mo-doped nitrogenated graphene structures. In each catalyst, the position of the Mo active site and the corresponding local carbon topologies are different, i.e. MoN_4C_{10} with in-plane Mo atom, MoN_4C_8 in which Mo atom bridges two adjacent armchair-like graphitic edges, and MoN_2C_3 in which Mo is doped at the edge of the graphene sheet. Using Density Functional Theory (DFT) calculations we discuss the electrocatalytic activity of Mo-N-C structures for nitrogen reduction reaction (NRR) with a focus on unraveling the corresponding mechanisms concerning different Mo site positions and C topologies. Our results indicate that the position of the active site centers has a great effect on its electrocatalytic behavior. The gas phase N_2 efficiently reduces to ammonia on MoN_4C_8 via the distal mechanism with an onset potential of -0.51 V. We confirm that the proposed pyridinic structure, MoN_4C_8, can catalyze NRR effectively with a low overpotential of 0.35 V.

Keywords: Electrocatalytic nitrogen reduction; Electrocatalysis; Single atom catalyst; Mo doped graphene

Introduction

Ammonia (NH_3), a carbon-free energy carrier [1], is known as one of the most essential chemicals. In the traditional Haber-Bosch process for the formation of ammonia, a large amount of energy consumes with massive emissions of carbon dioxide (CO_2). Therefore, developing other approaches to producing NH_3 is of great interest. Recently, the electrochemical nitrogen reduction reaction (NRR) is used as an alternative way for the formation of NH_3 under mild conditions using renewable sources of energy like solar or wind energy [2-4]. However, designing low-cost and high efficient electrocatalysts remains a big challenge [5-7].

Single-atom catalysts (SACs) are known as promising materials for a variety of (electro)catalytic reactions which are due to their high activity and selectivity [8-10]. Amongst, metal-doped pyridinic-N_4 embedded carbon materials are extensively studied for various catalytic purposes [11, 12]. In these catalysts, the transition metal doped N_4 (TM-N_4) is an active site while the surrounding carbon atoms stabilize the doped TM atom [13]. To date, the interest of theoretical and experimental investigations is to catalyze nitrogen fixation by heterogeneous catalysts, like Ru [14, 15], Pd [16, 17], or metal-free catalysts [18, 19]. The hydrogen evolution reaction (HER) is known as a competing reaction for NRR. HER leads to a low Faradaic efficiency (FE) [20, 21] and therefore, there is an urgent need to develop heterogeneous catalysts with significant activity and selectivity for catalyzing NRR.

Additionally, the topology of the local carbon atoms surrounding TM-N_4 active centers influences their electrocatalytic activity. The concept of the local carbon atoms was discovered in 2002 [22], 2007 [23], and rediscovered in 2008 [24] proposing a structure for most FeN_x/C active sites based on the previously proposed structures. Then, Lefèvre et al. [25] synthesized microporous carbon-supported Fe-based catalysts which were active toward oxygen reduction reaction (ORR). Lastly, in 2015, Jia et al. [26] and Nematollahi et al. [27], proposed that pyridinic FeN_4C_8 has great catalytic activity in the presence of a fifth ligand for catalytic ORR. However, recent reports indicated that Fe-N-C catalysts are considered as promising materials not only for ORR but also for NRR at room temperature [28, 29].

Molybdenum (Mo) is known to exhibit great potential for catalyzing NRR [30-34] and shows attractive catalytic properties [35, 36] confirmed by Nørskov et al. [37]. Recently, Mo-N-C electrocatalyst is synthesized and its catalytic activity is compared with the Fe, Mo-codoped hollow porous carbon nanorods for NRR [34]. Dessie et al. [38] successfully prepared nitrogen-doped defective carbon (Mo-N_4/d-C) with a high loading of 0.996 wt % via a designed vapor-deposition process for IOR-based hydrogen generation. This motivates us to investigate the electrocatalytic activity of three different types of MoN_xC_y catalysts with different local C topologies for NRR. We found that although all the

complexes can actively catalyze the NRR, the pyridinic MoN_4C_8 is more NRR active. Our results may help guide the experimental synthesis of highly efficient electrocatalysts for NRR or energy-conversion applications.

Computational details

DFT calculations. The spin-polarized DFT computations are performed using the Vienna ab initio simulation package (VASP) [39-41] with the Perdew-Burke-Ernzerhof (PBE) [42] functional for treating exchange-correlation effects. The projected augmented wave (PAW) method [43] is applied to describe the ion-electron interactions. A cutoff energy of 400 eV is chosen after checking the convergence energies with the convergence criterion of 10^{-6} eV and 0.01 eV/Å for the energy and force, respectively. The zero-damping Grimme approximation, DFT-D2, is used [44] to calculate the weak dispersion interactions (we found that the use of DFT-D3 dispersion [45] has negligible changes in the reaction coordinates of the order of 0.05 eV). Two different pyridinic MoN_4 models with different local carbon topologies, MoN_4C_8 and MoN_4C_{10}, along with Mo-doped graphene edges are constructed using VESTA [46]. A 4×3, 4×2, and 4×4 unit cell is used for MoN_4C_8, MoN_4C_{10}, and MoN_2C_3, respectively. The vacuum space is set to 15 Å in the z-direction. The Brillouin zones were sampled with a $5 \times 5 \times 1$ Monkhorst−Pack mesh.

The electrochemical N_2 reduction to ammonia, viz. $N_2 + 6H^+ + 6e^- \rightarrow 2NH_3$, involves six proton-coupled electron transfer steps. To calculate the reaction Gibbs free energy change (ΔG) for NRR processes we used the proposed computational hydrogen electrode (CHE) model by Nørskov et al. [47, 48]. In this model, the chemical potential of the proton-electron pair ($H^+ + e^-$) can be referenced to one-half of H_2 at standard reaction conditions. Therefore, the change in the free energy for each reaction step can be expressed according to the $\Delta G = \Delta E + \Delta ZPE - T\Delta S + \Delta G_{pH} + \Delta G_U$ equation. ΔE, ΔZPE, T, and ΔS are the calculated total energy, the change in the zero-point energy (ZPE), the temperature (in this work 298.15 K), and the entropy change, respectively. The VASPKIT code [49] is used to calculate the ΔZPE and ΔS values from vibrational frequency calculations. ΔG_{pH} refers to the free energy correction of the pH, $\Delta G_{pH} = k_B T \times pH \times \ln 10$ (or $0.059 \times PH$). The k_B in this equation refers to the Boltzmann constant and the value of pH is set to be 0. The free energy contribution related to the applied electrode potential (U) is shown with the ΔG_U term, i.e., $\Delta G_U = -neU$, where n and e are the numbers of $H^+ + e^-$ pairs transferred in NRR and the unit charge, respectively. Moreover, we calculate the limiting potential (U_{lim}) according to the $-\Delta G_{max}/e^-$ formula in which ΔG_{max} is related to the maximum free energy value obtained from an NRR step which determines the potential determining step (PDS). Finally, theoretical overpotential (η) can be calculated via the $\eta = U_{equ} - U_{lim}$ equation. U_{equ} refers to the equilibrium potential of NRR reaction, viz. -0.16 V vs. RHE [30, 50].

According to Nørskov et al. [51, 52] the stabilizations of adsorbed ORR intermediates on the Pt surface are between 0.25 and 0.5 eV while the stabilization of NRR intermediates is between 0.1 to 0.2 eV. Due to the similarity in the corrections, they suggested that shifts in activity might be related to the shifts along the scaling, and therefore, the fundamental boundaries are not changed dramatically from interactions with just H_2O. Thus, in this work, the solvation effect has not been included.

Results and discussions

Catalyst stability

Three different models involving Mo-doped pyridinic-N embedded graphene with various carbon topologies are investigated. In the MoN_4C_8 catalyst (complex A, Figure 1a), the MoN_4 site bridged two armchair-like graphitic edges. Although the MoN_4C_8 catalyst is not synthesized yet, recently, a similar configuration of this catalyst, FeN_4C_8, is synthesized [22, 23, 53] and theoretically modeled [26, 54, 55] by different groups. MoN_4C_{10} configuration is similar to the well-known metal-doped pyridinic N_4 embedded graphene which is the most stable representative of single metal atom doped N_4 catalysts (see complex B, Figure 1b). In this structure, the Mo atom is placed in-plane at the center of N_4 vacancy of the graphene sheet [11, 56-60]. Lastly, when the Mo atom binds with the edge-N atoms, the formed configuration is the MoN_2C_3 (complex C, Figure 1c).

Structural stability is an important requirement for electrocatalytic materials. This is closely related to their experimental fabrication and catalytic activity for long-term use [61]. Therefore, strong binding between the doped single metal atom and the anchoring substrate is very important to prohibit its diffusion and aggregation on the surface, which leads to different problems in SACs during operation. To address this, we here calculate the binding energy (E_b) of a single Mo atom anchored into the defective N_4 graphene, i.e. $E_b = E_{complex} - E_s - E_{Mo}$. $E_{complex}$, E_s, and E_{Mo} refer to the energy of the Mo-doped complex, defective $N_{4(2)}$ structure, and isolated Mo atom, respectively. The computed E_b for the MoN_4C_8, MoN_4C_{10}, and MoN_2C_3 complexes is -5.67, -6.60, and -3.76 eV, respectively. The negative E_b values strongly indicate that the doped Mo atom into the surrounding N_x vacancies has a low tendency to aggregate on the surface and therefore substantiate a good structural stability of the established models. Our results are comparable to previous investigations for similar NRR electrocatalysts [62-65]. The computed Mo−N bond length (d_{Mo-N}) of the optimized complexes is calculated to be in the range of 1.97−2.58 Å. As shown in Figure 1, the highest and lowest Mo-N bond length is related to complex B and C, respectively. According to the Bader charge analysis [66] in all the complexes, the Mo atom donors its electrons to the surrounding electronegative N atoms (see Table S1) and makes it positively charged. The charge transfer between Mo and the nearest neighboring N atoms is beneficial to stabilizing the Mo-N bonds, thereby confirming the structural stability of the

catalysts. One can see in Table S1 that more electrons are transferred from the catalysts to the surrounding N atoms from 1.17 to 1.20 e. We confirm the considerable charge distribution for Mo-N bond lenghes.
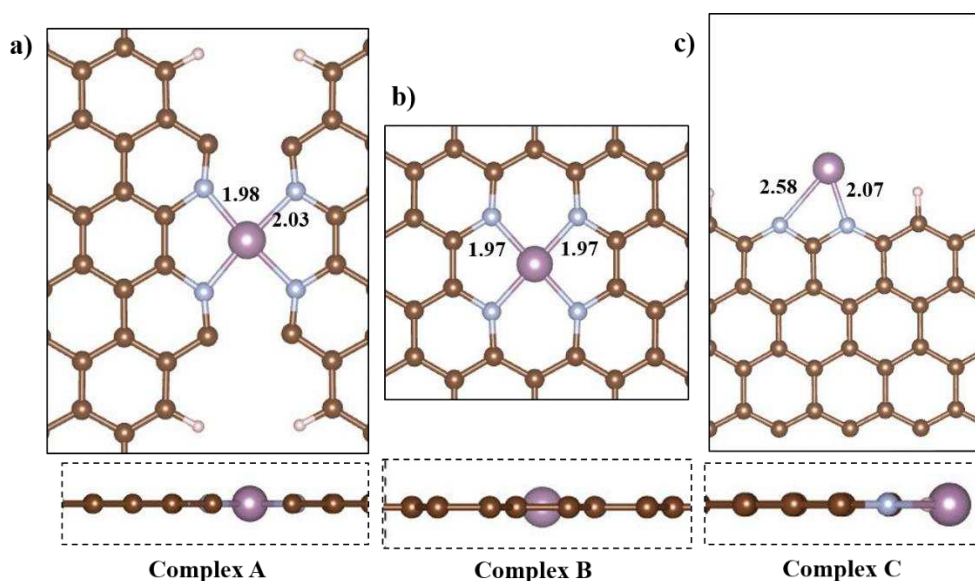
Figure 1. Proposed MoN_4C_8 (complex A), MoN_4C_{10} (complex B), and MoN_2C_3 (complex C) structures as representative Mo-N-C materials along with the corresponding Mo-N bond lengths. All the values are in Angstrom. Color code: brown, C; blue, N; purple, Mo; white, H

The electronic properties of the first two stable complexes are then calculated to obtain a reasonable description of electron distributions in solids that are beneficial for chemical bond classification. Figures 2a and 2b show the density of states (DOS) of complexes A and B along with their corresponding band structures, respectively. One can see that the DOS near the Fermi level is contributed by the Mo d-orbitals and the p-orbitals of N and C can be neglected. This confirms that the special coordination environment can improve the domination of d-electrons near the Fermi level and consequently can enhance the conductivity and catalytic activity of the complexes which is in favor of electrochemical NRR. A similar trend is reported for other Mo-doped N-embedded graphene structures [67].
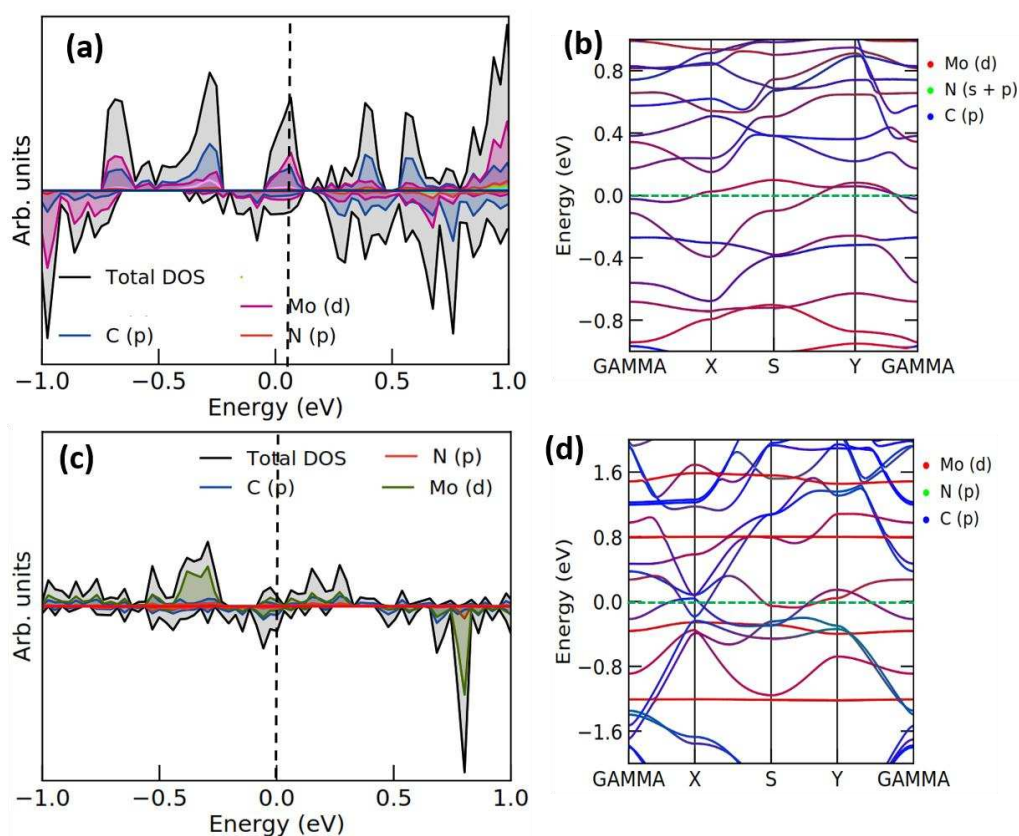
Figure 2. The calculated (a, c) density of states (DOS) and (b, d) band structure of complexes A and B. The Fermi level is set at 0.

Chemisorption and activation of N$_2$

*N$_2$ chemisorption and activation on the surface of the electrocatalyst is the first step of NRR and is crucial for the subsequent hydrogenation process [68]. Figure 3 illustrates the optimized configurations of *N$_2$ adsorbed on complexes A, B, and C via both end-on and side-on modes. The negative adsorption free energies of *N$_2$ imply its spontaneous chemisorption on all complexes, thereby validating the capability of the studied substrates for *N$_2$ adsorption and activation. Unlike complex B which adsorbs the *N$_2$ molecule with the same adsorption energy for both end-on and side-on modes, ΔE_{ads}= -2.2 eV, *N$_2$ adsorption predominantly adopts the end-on configuration on complexes A and C with ΔE_{ads}= -2.13 eV and ΔE_{ads} = -1.29 eV, respectively. The similar ΔE_{ads} for both *N$_2$ modes on complex B can be defined by calculating the Mo-N bond lengths. Generally, the longer the Mo-N bond, the weaker the interaction between the Mo atom and adsorbed *N$_2$ species (see table S2) and consequently, the lower the calculated adsorption energies. One can see in Table S2 that the obtained Mo-N bond length for both *N$_2$ modes on complex B is 1.96 Å. Therefore we can expect the similar ΔE_{ads} for these configurations wheras on complex A, the end-on *N$_2$ has the lowest Mo-N bond length and therefore has the highest ΔE_{ads}.

To further investigate the stability of the adsorbed configurations and *N$_2$ activation, the Bader

charge analysis is calculated. Our results reveal that upon *N_2 adsorption, the N-N bond increases in both the end-on and side-on modes, specifically in side-on configurations (see Figure 3). In all the configurations, the Mo unoccupied d-orbitals accept lone pairs or π-electron donation from adsorbed *N_2. However, the occupied d-orbitals of the Mo atom can back-donate electrons to the antibonding π* orbitals of *N_2. These electron transfers, weaken the strong triple N≡N bond and activate the N_2 species upon adsorption on the surface. This electron transfer is shown through the electron density difference (EDD) map confirming a great charge transfer from Mo to N atoms (see Table S2). Unlike the pure complexes A and B, upon *N_2 adsorption, more electrons transfer from these catalysts to the adsorbed *N_2, especially in side-on configurations. This can also be seen in complex C with lower and higher charge transfer for the end-on and side-on configurations, respectively. However, these great charge transfers lead to the N-N bond elongation, specifically in the side-on configurations where the N-N bond elongates from 1.10 Å in the free N_2 molecule to 1.23-1.27 Å. The significant charge transfer and N_2 activation confirm the strong chemisorption of *N_2 on the Mn center of the complexes mainly on complexes A and B. Our results are greater than the total electron transfer for *N_2 adsorption on Mo-doped boron nitride monolayer [69] indicating that the inert N_2 becomes more activated on MoN_x monolayers.
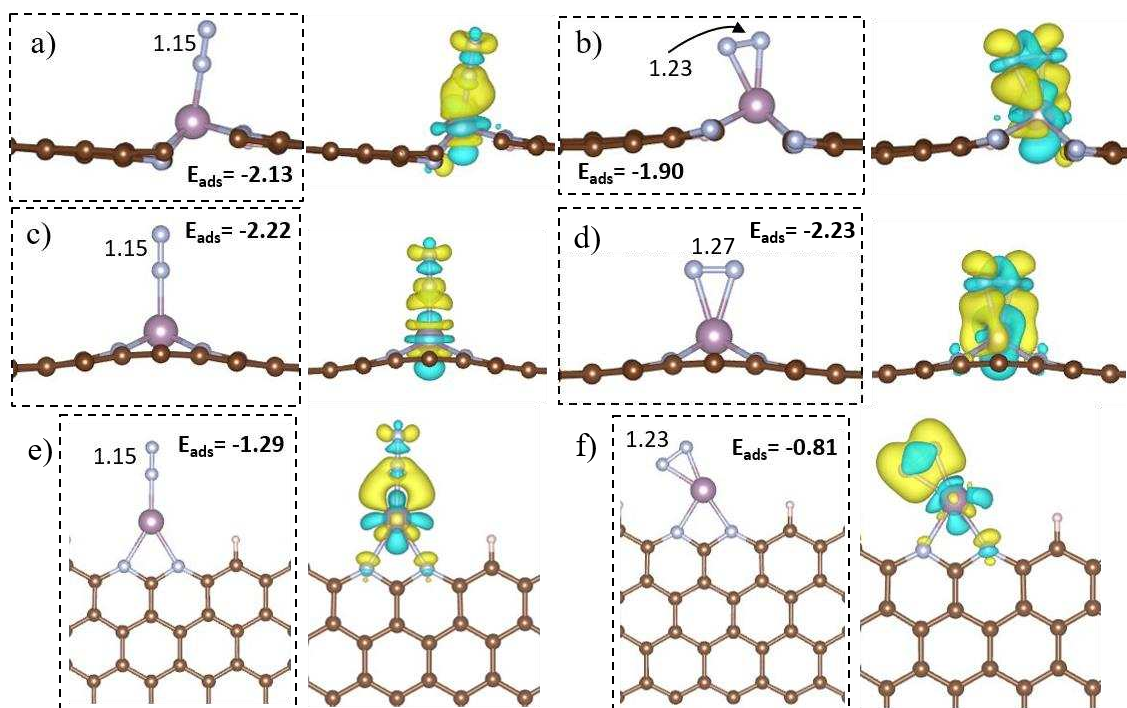
Figure 3. Optimized configurations of the *N_2 molecule adsorbed on complexes A, B, and C via end-on (a, c, e) and side-on (b, d, f) pattern along with the corresponding electron density difference (EDD) map. The charge accumulation and depletion are displayed by the yellow and cyan region with the isosurface value of 0.004 e/Å^3. The bond lengths and adsorption energy values are in Å and eV, respectively. Color code: brown, C; blue, N; purple, Mo; white, H

To gain a better physical insight into the pure complexes and adsorbed configurations, we analyzed

the DOS of $*N_2$ on the Mo atom of complexes A and B (Figure S1). The DOS plots demonstrated that on both $*N_2$ orientations, a considerable broadening of antibonding orbitals occurs, showing a great electron donation and back-donation of the catalysts (Figures S1i-l). Moreover, one can see in Figures S1c-f that upon adsorption of $*N_2$ on the Mo atom of complexes A and B, the contribution of the Mo d-orbitals and N p-orbitals increases by forming sharper peaks near the Fermi energy.

Electrocatalytic reduction of N_2

**Screening the MoN_xC_x complexes as NRR electrocatalysts**

The adsorption configuration of $*N_2$ defines the pathway in which the $*N_2$ reduces to NH_3/NH_4^+. It is well-established that the NRR proceeds via three pathways, namely distal, alternating, and enzymatic. The NRR pathways proceed in accordance with the adsorbed $*N_2$ configuration that can be either end-on (required for distal and alternating mechanisms) or side-on (required for enzymatic pathway). According to previous investigations [37, 70], two stable to unstable transitions are found in the NRR process: the first ($*N_2 \rightarrow *NNH$) and the last hydrogenation step ($*NH_2 \rightarrow *NH_3$). The reason is that $*N_2$ is a stable molecule and breaking its triplet N≡N bond requires a large energy change which makes the first hydrogenation reaction endergonic. In the last hydrogenation step, the $*NH_2$ species tends to be stabilized on the Mo active center of the catalysts by converting to $*NH_3$. In contrast, in $*NH_3$, all the hybrid orbitals are filled and thus making it unstable on the surface, compared to $*NH_2$. Thus, the formation of $*NH_3$ should also be endergonic while the hydrogenation of other intermediates is estimated to be exergonic [71, 72]. Therefore, we screened these two reactions on each catalyst and calculated the corresponding free energy of the reaction, ΔG_{N2-NNH}, and $\Delta G_{NH2-NH3}$ as the activity descriptor. In addition, the adsorption energy of $*N_2$ is also considered because the chemisorption and activation of $*N_2$ on the catalyst's surface are also crucial [37] (see Figure 4a). To ensure that the limiting potential is close to that of the best transition metal [37, 73] we studied the NRR on the catalysts with both ΔG_{N2-NNH} and $\Delta G_{NH2-NH3}$ values lower than 0.60 eV (see Figure 4b). One can see that complex A looks more suitable for NRR while complexes B and C require for about 0.04 and 0.05 eV more free energy than the determined threshold value reported for catalyzing the first and last

hydrogenation steps and can be neglected. Therefore, in this work, we further screened out the NRR mechanisms on all the studied catalysts.
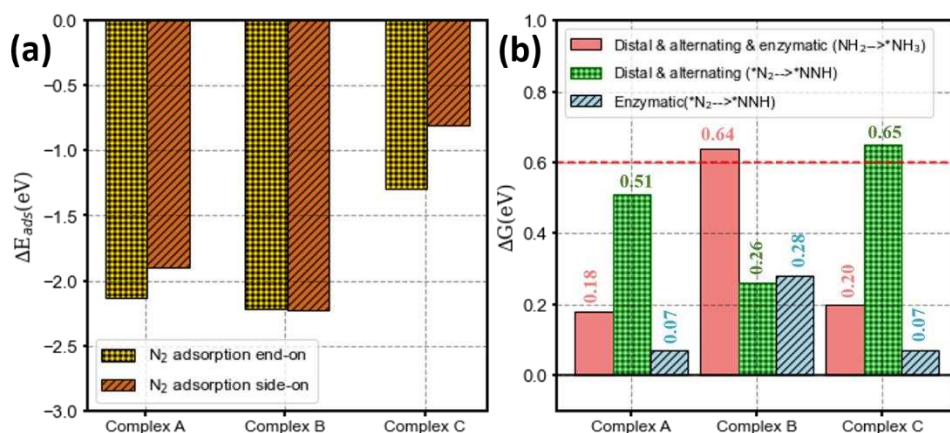
Figure 4. *N_2 adsorption energy (a) and Gibbs free energy changes for the hydrogenation of *N_2 and *NH_2 intermediates (b) on complexes A, B, and C

We then investigated the dital, alternating, and enzymatic mechanisms on complexes A, B, and C and the corresponding ΔG_{max} for each pathway is plotted and shown in Figure 5. One can see that all the complexes can catalyze NRR with ΔG_{max} lower than < 1 eV except for the enzymatic mechanism on complexes A and B with ΔG_{max} > 1 eV (below the black dashed line). However, the distal/alternating mechanisms on complexes A/C and distal mechanism on complex B requires ΔG_{max} < 0.75 eV (below the red dashed line) while the alternating mechanism on complex B and the enzymatic mechanism on complex C requires 0.75 eV < ΔG_{max} < 1 eV. Therefore, in the following sections, we mainly focus on the mechanisms with ΔG_{max} < 0.75 eV and the reaction mechanisms with ΔG_{max} > 1 eV and 0.75 eV < ΔG_{max} < 1 eV are plotted and shown in Figures S2-S4 in the Supporting Information.
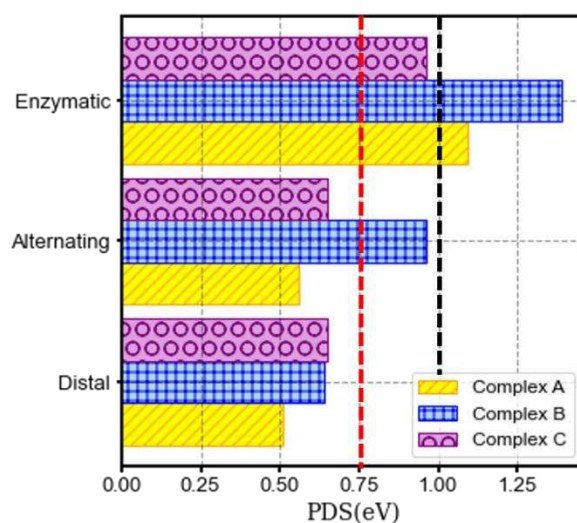

Figure 5. Computed reaction free energy for distal, alternating, and enzymatic pathways on complexes A, B, and C. Each catalyst is depicted in different colors

NRR on complex A

We plotted the free energy diagrams for NRR on complex A in Figure 6. In each step of the NRR mechanism, the proton/electron pairs are transferred to the electrode surface which results in the consecutive hydrogenation of nitrogen species forming different reaction intermediates, depending on the ongoing mechanism, and finally the formed NH_3 releases from the surface at two different steps. In the distal mechanism, the first NH_3 molecule produces directly after the first three hydrogenation steps forming *NNH, *NNH_2, and *N species on the active MoN_4 site, whereas the second NH_3 molecule forms at the last step, when the next three proton/electron pairs attack the remained *N atom forming *NH, *NH_2, and *NH_3 intermediates. In contrast, in the alternating and enzymatic mechanisms, the proton/electron pairs interact with two N atoms of the adsorbed *N_2 alternatively. As mentioned in the previous section, the only difference between these two pathways is the adsorption configuration of adsorbed *N_2.

As expected, in the distal mechanism, the first hydrogenation of *N_2 is thermodynamically unfavorable with $\Delta G_{*N2-*NNH}$ = 0.51 eV at zero potential. Subsequently, the *H species interacts with the terminal N atom and forms *NNH_2. The first NH_3 molecule is released from the surface in the third hydrogenation step and *N remains on the surface. In all of the hydrogenation steps, the N-N bond length increases from 1.10 Å in the gas phase N_2 to 1.35 Å in *NNH_2 species (see Figure 6a). The next three hydrogenation steps are required to produce the second NH_3 molecule from *N protonation, forming *NH, *NH_2, and *NH_3 on the Mo active site of the catalyst. The addition of proton/electron pairs in each step leads to the elongation of Mo-N bond length from 1.68 Å in *N configuration to 1.95 Å and 2.24 Å in *NH_2 and *NH_3 configurations, respectively. According to previous investigations [74, 75], the adsorbed *NH_3 species is easily protonated to *NH_4^+ under electrochemical conditions. Therefore, here, we do not discuss this protonation step in detail. Up to now, all hydrogenation steps are downhill except for the formation of *NH_2 and *NH_3 with a surmountable free energy value at ambient conditions. One can see in Figure 6a that the formation of the second *NH_3 requires lower free energy ($\Delta G_{*NH2-*NH3}$=0.18 eV) than the formation of *NNH ($\Delta G_{*N2-*NNH}$=0.51 eV). Therefore, the protonation of *N_2 is the PDS in the distal mechanism with a limiting potential of U_{lim}= -0.51 V vs SHE. The calculated overpotential for the distal mechanism is η = 0.35 V.
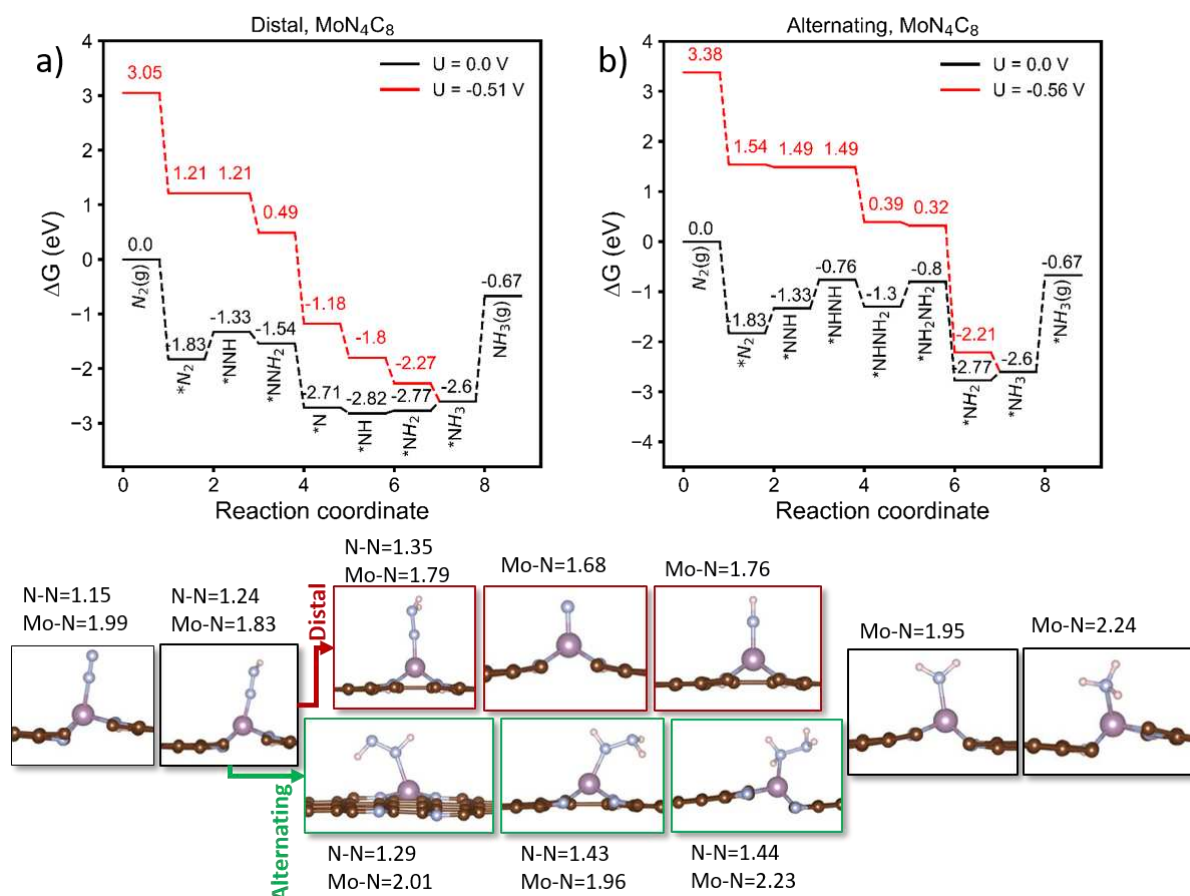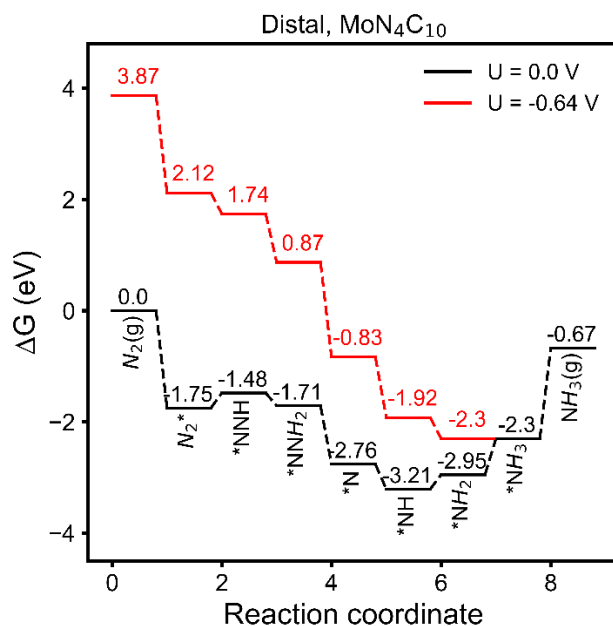
Figure 6. Free energy profiles for NRR on complex A through distal (a) and alternating (b) mechanisms at zero and applied potentials along with the corresponding optimized configurations. Color code: brown, C; blue, N; purple, Mo; white, H

In the alternating pathway, the protonation steps occur alternatively on *N atoms. Additionally, the first and second NH_3 molecule forms and desorbs from the catalyst in the fifth and sixth protonation steps, respectively. Compared to the distal mechanism, in the second hydrogenation step, the N-N bond elongation is lower, N-N = 1.29 Å, in the alternating pathway than that in the distal mechanism, N-N = 1.35 Å. In the next hydrogenation steps, the N-N bond increases to 1.44 Å until the first NH_3 molecule forms and is released from the surface. One can see in Figure 6b that except for *N_2 protonation which is similar to that of the distal mechanism, the second, fourth, and last hydrogenation steps are uphill with $\Delta G_{*NNH-*NHNH} = 0.56$ eV, $\Delta G_{*NHNH2-*NH2NH2} = 0.50$ eV, and $\Delta G_{*NH2-*NH3} = 0.17$ eV, respectively. Among the endothermic reactions, the highest free energy change is for the formation of *NHNH species which is identified as the PDS with -0.56 V vs HSE and $\eta = 0.40$ V.

NRR on complex B

NRR proceeds with lower U_{lim} on complex B (U_{lim} = -0.64 V) via the distal mechanism (Figure 7) than that of alternating (U_{lim} = -0.96 V) and enzymatic (U_{lim} = -1.39 V) mechanisms shown in Figure S3a,b. In the distal mechanism, the first, fifth, and sixth hydrogenation steps are endothermic with the ΔG_{*N2-}

$_{*NNH}$ = 0.26 eV, $\Delta G_{*NH-*NH2}$ = 0.26 eV, and $\Delta G_{*NH2-*NH3}$ = 0.64 eV, respectively. The formation of *NH$_3$ is considered as the PDS with the higher reaction free energy value and η is calculated to be 0.48 V.
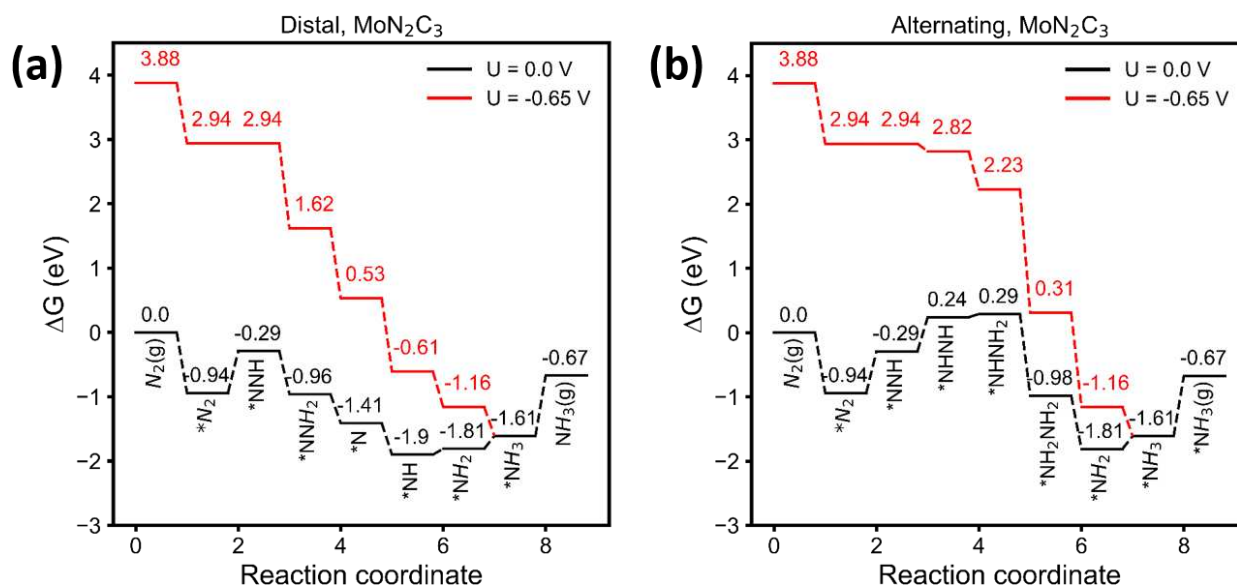

Figure 7. Free energy profiles for NRR on complex B through distal mechanism at zero and applied potentials

NRR on complex C

The electrocatalytic activity of the Mo-doped nitrogenated edges of the catalyst is investigated carefully for NRR. As shown in Figure 5, distal and alternating mechanisms of NRR on complex C have lower ΔG_{max} values than that of the enzymatic mechanism. Therefore, in the following, we report on the first two mechanisms, and the free energy plot of the enzymatic pathway is shown and explained in Figure S4 of the Supporting Information.

One can see in Figure 8a that in the distal pathway, the formation of *NNH, *NH$_2$, and *NH$_3$ is endothermic at zero potential. While the latter two reactions are slightly endothermic with $\Delta G_{*NH-*NH2}$ = 0.09 eV and $\Delta G_{*NH2-*NH3}$ = 0.20 eV, the first hydrogenation of *N$_2$ has the maximum reaction free energy of $\Delta G_{*N2-*NNH}$ = 0.65 eV making this reaction the PDS with the overpotential of 0.49 V. Like the distal mechanism, the first hydrogenation reaction is the PDS in the alternating mechanism with the same U_{lim} and η value. As shown in Figure 8b, all the reaction steps are downhill except for the formation of *NHNH, *NHNH$_2$, and *NH$_3$ from which the formation of *NHNH has the second high ΔG value of 0.53 eV.

Figure 8. Free energy profiles for NRR on complex C through distal (a) and alternating (b) mechanisms at zero and applied potentials

HER Selectivity

To understand the catalytic activity of a complex for NRR, its selectivity for the competing reactions should also be investigated. Hydrogen evolution reaction (HER, $2H^+ + 2e^- \rightarrow H_2$, $E^0 = 0$ V) is known as a coupling reaction to NRR and should be suppressed to improve the selectivity of nitrogen fixation [76]. HER is an important issue that hinders the development of efficient electrocatalysts [51, 77]. Generally, in an acidic environment, HER consumes a significant amount of H^+/e^- pairs. Therefore, there might be a possibility of the catalysts' active site occupancy, which leads to the production of H_2 at similar limiting potentials as for NRR, consequently, reducing the Faraday efficiency (FE) [68, 78]. Therefore, to compare the HER activity with NRR, we computed the Gibbs free energy of adsorption for $*N_2$ ($\Delta G_{ad(N2)}$) and $*H (\Delta G_{ad(H)})$ on the Mo active site of each catalyst and shown in Figures 9a and 9b, respectively. In Figure 9b, the catalysts in the green area are NRR-selective. According to our results, we confirm that the N_2 adsorption is more favorable in all of the studied complexes than the $*H$ adsorption, and therefore, complex A with higher (more negative) calculated E_{ads} for N_2 and lower onset potential is the most selective catalyst for NRR.
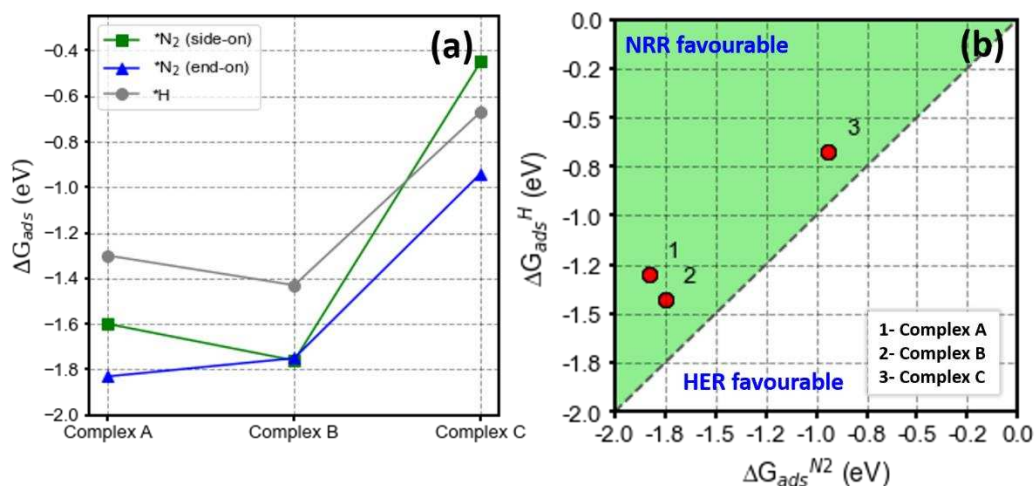
Figure 9. (a) *N_2 and *H free energy of adsorption on complexes A, B, and C. (b) Free energy of adsorption for *H and *N_2 on complexes A, B, and C where the catalysts in the green region are NRR selective

Moreover, since the NRR is conducted in aqueous electrolytes, H_2O* species can poison the metal active sites of the surface. Therefore, we calculated the adsorption energy of water on the Mo site of the studied complexes as follows:

$$E_{ads} = E_{H2O@catalyst} - E_{catalyst} - E_{H2O} - 2E_{H\text{-}bond} \tag{1}$$

where $E_{H2O@catalyst}$, $E_{catalyst}$, and E_{H2O} correspond to the total energies of the adsorbed water on the catalyst, the pure catalyst, and the molecular H_2O, respectively. It is known that water molecules form four hydrogen bonds in water [79] with the total hydrogen binding energy of $E_{H\text{-}bond} = -0.26$ eV. Upon adsorption of water molecules on the active center of the catalyst, the adsorbed H_2O* can only have two other hydrogen bonds with the presented water molecules in the solution. Thus, it is necessary to consider two hydrogen bond cleavages in the H_2O adsorption energy calculation. One can see in Table S2 that the adsorption energy of H_2O* in all complexes is lower than that of *N_2 indicating that the active sites are mainly covered with *N_2 rather than H_2O* species. Our findings are in good agreement with the previous report by Zhao et al. [80].

Conclusion

In summary, we investigated the activity and selectivity of NRR on two types of pyridinic MoN_4 doped graphene with different carbon topologies, MoN_4C_8 and MoN_4C_{10}, and MoN_2C_3 at the edge of micropores, using DFT calculations. Our results reveal that all three catalysts can reduce nitrogen with onset potentials <1.5 V. Amongst, MoN_4C_8 catalyzes the N_2 reduction with the lowest onset potential of -0.51 V vs HSE via the distal mechanism. The stable structure, MoN_4C_{10}, binds strongly with *N_2 species leading to a higher NRR onset potential of -0.64 V vs HSE through the distal mechanism. Complex C can catalyze NRR via the distal and alternating mechanisms with the $U_{lim} = -0.65$ V. Our investigation indicate that the position of the active site centers has a great effect on the electrocatalytic behavior of

the used catalyst. This work provides a comprehensive understanding of the structural stability, electrocatalytic activity, and selectivity of Mo-N-C catalysts with different C topologies and active site positions. It also opens up the way to utilize the newly proposed MoN_4-C_8 electrocatalyst for energy-conversion and electrocatalysis applications.

Supporting information

The DOS plot for pure complex A (a, g), pure complex B (b, h), end-on $*N_2$ adsorbed on complex A (c, i), end-on $*N_2$ adsorbed on complex B (d, j), side-on $*N_2$ adsorbed on complex A (e, k), and side-on adsorbed $*N_2$ on complex B (f, l); The NRR through the enzymatic pathway on complexes A at zero and applied potential along with the corresponding optimized configurations. Color code: brown, C; blue, N; purple, Mo; and white, H; The NRR through the alternating (a) and enzymatic (b) pathways on complex B at zero and applied potential; The NRR through enzymatic pathway on complexes C at zero and applied potential; The computed Bader charge (q) on Mo and N atoms in complexes A, B, and C along with the E_b of Mo atom into the surface; The computed Bader charge (q) on Mo atom and adsorbed $*N_2$ species on complexes A, B, and C along with the corresponding adsorption energies (ΔE_{ads}) and Mo-N bond length.

Author declarations

Conflict of interest

The authors have no conflicts to disclose.

References

[1] J.G. Chen, R.M. Crooks, L.C. Seefeldt, K.L. Bren, R.M. Bullock, M.Y. Darensbourg, P.L. Holland, B. Hoffman, M.J. Janik, A.K. Jones, Beyond fossil fuel–driven nitrogen transformations, Science, 360 (2018) eaar6611.

[2] A.J. Martín, J. Pérez-Ramírez, Heading to distributed electrocatalytic conversion of small abundant molecules into fuels, chemicals, and fertilizers, Joule, 3 (2019) 2602-2621.

[3] V. Kyriakou, I. Garagounis, A. Vourros, E. Vasileiou, M. Stoukides, An electrochemical haber-bosch process, Joule, 4 (2020) 142-158.

[4] G. Soloveichik, Electrochemical synthesis of ammonia as a potential alternative to the Haber–Bosch process, Nature Catalysis, 2 (2019) 377-380.

[5] H. Liu, L. Wei, F. Liu, Z. Pei, J. Shi, Z.-j. Wang, D. He, Y. Chen, Homogeneous, heterogeneous, and biological catalysts for electrochemical N2 reduction toward NH3 under ambient conditions, ACS Catal., 9 (2019) 5245-5267.

[6] A.R. Singh, B.A. Rohr, M.J. Statt, J.A. Schwalbe, M. Cargnello, J.K. Nørskov, Strategies toward selective electrochemical ammonia synthesis, ACS Catal., 9 (2019) 8316-8324.

[7] B.H. Suryanto, H.-L. Du, D. Wang, J. Chen, A.N. Simonov, D.R. MacFarlane, Challenges and prospects in the catalysis of electroreduction of nitrogen to ammonia, Nature Catalysis, 2 (2019) 290-296.

[8] H.J. Qiu, Y. Ito, W. Cong, Y. Tan, P. Liu, A. Hirata, T. Fujita, Z. Tang, M. Chen, Nanoporous graphene with single‐atom nickel dopants: an efficient and stable catalyst for electrochemical hydrogen production, Angew. Chem., 54 (2015) 14031-14035.

[9] S. Back, J. Lim, N.-Y. Kim, Y.-H. Kim, Y. Jung, Single-atom catalysts for CO 2 electroreduction with significant activity and selectivity improvements, Chemical science, 8 (2017) 1090-1096.

[10] H. Niu, Z. Zhang, X. Wang, X. Wan, C. Shao, Y. Guo, Theoretical Insights into the Mechanism of Selective Nitrate‐to‐Ammonia Electroreduction on Single‐Atom Catalysts, Adv. Funct. Mater., 31 (2021) 2008533.

[11] K.L. Svane, M. Reda, T. Vegge, H.A. Hansen, Improving the Activity of M− N4 Catalysts for the Oxygen Reduction Reaction by Electrolyte Adsorption, ChemSusChem, 12 (2019) 5133-5141.

[12] M. Abel, S. Clair, O. Ourdjini, M. Mossoyan, L. Porte, Single layer of polymeric Fe-phthalocyanine: an organometallic sheet on metal and thin insulating film, Journal of the American Chemical Society, 133 (2011) 1203-1205.

[13] O.A. Melville, B.H. Lessard, T.P. Bender, Phthalocyanine-based organic thin-film transistors: a review of recent advances, ACS Appl. Mater. Interfaces, 7 (2015) 13105-13118.

[14] Z. Geng, Y. Liu, X. Kong, P. Li, K. Li, Z. Liu, J. Du, M. Shu, R. Si, J. Zeng, Achieving a record‐high yield rate of 120.9 for N2 electrochemical reduction over Ru single‐atom catalysts, Adv. Mater., 30 (2018) 1803498.

[15] D. Wang, L.M. Azofra, M. Harb, L. Cavallo, X. Zhang, B.H. Suryanto, D.R. MacFarlane, Energy‐efficient nitrogen reduction to ammonia at low overpotential in aqueous electrolyte under ambient conditions, ChemSusChem, 11 (2018) 3416-3422.

[16] L. Zhang, X. Ren, Y. Luo, X. Shi, A.M. Asiri, T. Li, X. Sun, Ambient NH 3 synthesis via electrochemical reduction of N 2 over cubic sub-micron SnO 2 particles, ChemComm, 54 (2018) 12966-12969.

[17] J. Wang, L. Yu, L. Hu, G. Chen, H. Xin, X. Feng, Ambient ammonia synthesis via palladium-catalyzed electrohydrogenation of dinitrogen at low overpotential, Nat. Commun., 9 (2018) 1-7.

[18] C. Lv, Y. Qian, C. Yan, Y. Ding, Y. Liu, G. Chen, G. Yu, Defect engineering metal‐free polymeric carbon nitride electrocatalyst for effective nitrogen fixation under ambient conditions, Angew. Chemi., 130 (2018) 10403-10407.

[19] X. Yu, P. Han, Z. Wei, L. Huang, Z. Gu, S. Peng, J. Ma, G. Zheng, Boron-doped graphene for electrocatalytic N2 reduction, Joule, 2 (2018) 1610-1622.

[20] X. Cui, C. Tang, Q. Zhang, A review of electrocatalytic reduction of dinitrogen to ammonia under ambient conditions, Advanced Energy Materials, 8 (2018) 1800369.

[21] Z.W. Seh, J. Kibsgaard, C.F. Dickens, I. Chorkendorff, J.K. Nørskov, T.F. Jaramillo, Combining theory and experiment in electrocatalysis: Insights into materials design, Science, 355 (2017) eaad4998.

[22] M. Lefèvre, J. Dodelet, P. Bertrand, Molecular oxygen reduction in PEM fuel cells: evidence for the simultaneous presence of two active sites in Fe-based catalysts, J. Phys. Chem. B., 106 (2002) 8705-8713.

[23] J.H. Zagal, F. Bedioui, J.-P. Dodelet, N4-macrocyclic metal complexes, Springer Science & Business Media, 2007.

[24] F. Charreteur, F. Jaouen, S. Ruggeri, J.-P. Dodelet, Fe/N/C non-precious catalysts for PEM fuel cells: Influence of the structural parameters of pristine commercial carbon blacks on their activity for oxygen reduction, Electrochim. Acta, 53 (2008) 2925-2938.

[25] M. Lefèvre, E. Proietti, F. Jaouen, J.-P. Dodelet, Iron-based catalysts with improved oxygen reduction activity in polymer electrolyte fuel cells, Science, 324 (2009) 71-74.

[26] Q. Jia, N. Ramaswamy, H. Hafiz, U. Tylus, K. Strickland, G. Wu, B. Barbiellini, A. Bansil, E.F. Holby, P. Zelenay, Experimental observation of redox-induced Fe–N switching behavior as a determinant role for oxygen reduction activity, ACS Nano, 9 (2015) 12496-12505.

[27] P. Nematollahi, B. Barbiellini, A. Bansil, D. Lamoen, J. Qingying, S. Mukerjee, E.C. Neyts, Identification of a Robust and Durable FeN4C x Catalyst for ORR in PEM Fuel Cells and the Role of the Fifth Ligand, ACS Catal., 12 (2022) 7541-7549.

[28] X. Guo, S. Huang, Tuning nitrogen reduction reaction activity via controllable Fe magnetic moment: A computational study of single Fe atom supported on defective graphene, Electrochim. Acta, 284 (2018) 392-399.

[29] X.-F. Li, Q.-K. Li, J. Cheng, L. Liu, Q. Yan, Y. Wu, X.-H. Zhang, Z.-Y. Wang, Q. Qiu, Y. Luo, Conversion of dinitrogen to ammonia by FeN3-embedded graphene, Journal of the American Chemical Society, 138 (2016) 8706-8709.

[30] S. Agarwal, R. Kumar, R. Arya, A.K. Singh, Rational Design of Single-Atom Catalysts for Enhanced Electrocatalytic Nitrogen Reduction Reaction, J. Phys. Chem. C., 125 (2021) 12585-12593.

[31] L. Li, J.M.P. Martirez, E.A. Carter, Prediction of highly selective electrocatalytic nitrogen reduction at low overpotential on a Mo-doped g-GaN monolayer, ACS Catal., 10 (2020) 12841-12857.

[32] C. Ling, X. Bai, Y. Ouyang, A. Du, J. Wang, Single molybdenum atom anchored on N-doped carbon as a promising electrocatalyst for nitrogen reduction into ammonia at ambient conditions, J. Phys. Chem. C., 122 (2018) 16842-16847.

[33] Y. Zhang, J. Hu, C. Zhang, A.T. Cheung, Y. Zhang, L. Liu, M.K. Leung, Mo2C embedded on nitrogen-doped carbon toward electrocatalytic nitrogen reduction to ammonia under ambient conditions, Int. J. Hydrogen Energ., 46 (2021) 13011-13019.

[34] W. Ye, Y. Yang, M. Arif, S. Yang, X. Fang, M.A. Mushtaq, X. Chen, D. Yan, Fe, Mo–N/C hollow porous nitrogen-doped carbon nanorods as an effective electrocatalyst for N2 reduction reaction, ACS Sustainable Chemistry & Engineering, 8 (2020) 15946-15952.

[35] Z. Zhuang, J. Huang, Y. Li, L. Zhou, L. Mai, The Holy Grail in Platinum‐Free Electrocatalytic Hydrogen Evolution: Molybdenum‐Based Catalysts and Recent Advances, ChemElectroChem, 6 (2019) 3570-3589.

[36] R. Ge, J. Huo, M. Sun, M. Zhu, Y. Li, S. Chou, W. Li, Surface and interface engineering: molybdenum carbide–based nanomaterials for electrochemical energy conversion, Small, 17 (2021) 1903380.

[37] E. Skulason, T. Bligaard, S. Gudmundsdóttir, F. Studt, J. Rossmeisl, F. Abild-Pedersen, T. Vegge, H. Jónsson, J.K. Nørskov, A theoretical evaluation of possible transition metal electro-catalysts for N

2 reduction, Phys. Chem. Chem. Phys., 14 (2012) 1235-1245.

[38] T.A. Dessie, W.-H. Huang, D.B. Adam, Y.A. Awoke, C.-H. Wang, J.-L. Chen, C.-W. Pao, N.G. Habtu, M.-C. Tsai, W.-N. Su, Efficient H2 Evolution Coupled with Anodic Oxidation of Iodide over Defective Carbon-Supported Single-Atom Mo-N4 Electrocatalyst, Nano Lett., (2022).

[39] G. Kresse, J. Hafner, Ab initio molecular dynamics for liquid metals, Phys. Rev. B, 47 (1993) 558.

[40] J. Perdew, K. Burke, M. Ernzerhof, D. of physics and NOL 70118 J. quantum theory group tulane university, Phys. Rev. Lett, 77 (1996) 3865-3868.

[41] G. Kresse, J. Furthmüller, Efficiency of ab-initio total energy calculations for metals and semiconductors using a plane-wave basis set, Comput. Mater. Sci., 6 (1996) 15-50.

[42] J.P. Perdew, J.A. Chevary, S.H. Vosko, K.A. Jackson, M.R. Pederson, D.J. Singh, C. Fiolhais, Atoms, molecules, solids, and surfaces: Applications of the generalized gradient approximation for exchange and correlation, Phys. Rev. B, 46 (1992) 6671.

[43] P.E. Blöchl, Projector augmented-wave method, Phys. Rev. B, 50 (1994) 17953.

[44] T. Bucko, J. Hafner, S. Lebegue, J.G. Angyán, Improved description of the structure of molecular and layered crystals: ab initio DFT calculations with van der Waals corrections, J. Phys. Chem. A., 114 (2010) 11814-11824.

[45] S. Grimme, J. Antony, S. Ehrlich, H. Krieg, A consistent and accurate ab initio parametrization of density functional dispersion correction (DFT-D) for the 94 elements H-Pu, J. Chem. Phys., 132 (2010) 154104.

[46] K. Momma, F. Izumi, VESTA: a three-dimensional visualization system for electronic and structural analysis, Journal of Applied crystallography, 41 (2008) 653-658.

[47] J.K. Nørskov, J. Rossmeisl, A. Logadottir, L. Lindqvist, J.R. Kitchin, T. Bligaard, H. Jonsson, Origin of the overpotential for oxygen reduction at a fuel-cell cathode, J. Phys. Chem. B., 108 (2004) 17886-17892.

[48] A.A. Peterson, F. Abild-Pedersen, F. Studt, J. Rossmeisl, J.K. Nørskov, How copper catalyzes the electroreduction of carbon dioxide into hydrocarbon fuels, Energy Environ. Sci., 3 (2010) 1311-1315.

[49] V. Wang, N. Xu, J.-C. Liu, G. Tang, W.-T. Geng, VASPKIT: A user-friendly interface facilitating high-throughput computing and analysis using VASP code, Computer Physics Communications, 267 (2021) 108033.

[50] Y. Cao, S. Deng, Q. Fang, X. Sun, C. Zhao, J. Zheng, Y. Gao, H. Zhuo, Y. Li, Z. Yao, Single and double boron atoms doped nanoporous C2N–h2D electrocatalysts for highly efficient N2 reduction reaction: a density functional theory study, Nanotechnology, 30 (2019) 335403.

[51] J.H. Montoya, C. Tsai, A. Vojvodic, J.K. Nørskov, The challenge of electrochemical ammonia synthesis: a new perspective on the role of nitrogen scaling relations, ChemSusChem, 8 (2015) 2180-2186.

[52] V. Tripković, E. Skúlason, S. Siahrostami, J.K. Nørskov, J. Rossmeisl, The oxygen reduction reaction mechanism on Pt (111) from density functional theory calculations, Electrochim. Acta, 55 (2010) 7975-7981.

[53] A. Bouwkamp-Wijnoltz, W. Visscher, J. Van Veen, E. Boellaard, A. Van der Kraan, S. Tang, On active-site heterogeneity in pyrolyzed carbon-supported iron porphyrin catalysts for the electrochemical reduction of oxygen: an in situ Mössbauer study, J. Phys. Chem. B., 106 (2002) 12993-13001.

[54] K. Liu, G. Wu, G. Wang, Role of Local Carbon Structure Surrounding FeN4 Sites in Boosting the Catalytic Activity for Oxygen Reduction, J. Phys. Chem. C., 121 (2017) 11319-11324.

[55] A. Zitolo, V. Goellner, V. Armel, M.-T. Sougrati, T. Mineva, L. Stievano, E. Fonda, F. Jaouen, Identification of catalytic sites for oxygen reduction in iron-and nitrogen-doped graphene materials, Nat. Mater., 14 (2015) 937-942.

[56] A.B. Anderson, E.F. Holby, Pathways for O2 Electroreduction over Substitutional FeN4, HOFeN4, and OFeN4 in Graphene Bulk Sites: Critical Evaluation of Overpotential Predictions Using

LGER and CHE Models, J. Phys. Chem. C., 123 (2019) 18398-18409.

[57] N. Mohd Adli, W. Shan, S. Hwang, W. Samarakoon, S. Karakalos, Y. Li, D.A. Cullen, D. Su, Z. Feng, G. Wang, Engineering Atomically Dispersed FeN4 Active Sites for CO2 Electroreduction, Angew. Chem., Int. Ed., 133 (2021) 1035.

[58] P. Nematollahi, E.C. Neyts, Direct methane conversion to methanol on M and MN4 embedded graphene (M= Ni and Si): A comparative DFT study, Appl. Surf. Sci., 496 (2019) 143618.

[59] Z. Lu, M. Yang, D. Ma, P. Lv, S. Li, Z. Yang, CO oxidation on Mn-N4 porphyrin-like carbon nanotube: A DFT-D study, Appl. Surf. Sci., 426 (2017) 1232-1240.

[60] X. Zhang, Z. Lu, Z. Yang, The mechanism of oxygen reduction reaction on CoN4 embedded graphene: A combined kinetic and atomistic thermodynamic study, Int. J. Hydrogen Energ., 41 (2016) 21212-21220.

[61] C. Choi, S. Back, N.-Y. Kim, J. Lim, Y.-H. Kim, Y. Jung, Suppression of hydrogen evolution reaction in electrochemical N2 reduction using single-atom catalysts: a computational guideline, ACS Catal., 8 (2018) 7517-7525.

[62] X. Lv, W. Wei, F. Li, B. Huang, Y. Dai, Metal-free B@ g-CN: visible/infrared light-driven single atom photocatalyst enables spontaneous dinitrogen reduction to ammonia, Nano Lett., 19 (2019) 6391-6399.

[63] T. Yang, T.T. Song, J. Zhou, S. Wang, D. Chi, L. Shen, M. Yang, Y.P. Feng, High-throughput screening of transition metal single atom catalysts anchored on molybdenum disulfide for nitrogen fixation, Nano Energy, 68 (2020) 104304.

[64] C. Ren, Q. Jiang, W. Lin, Y. Zhang, S. Huang, K. Ding, Density functional theory study of single-atom V, Nb, and Ta catalysts on graphene and carbon nitride for selective nitrogen reduction, ACS Applied Nano Materials, 3 (2020) 5149-5159.

[65] Z. Wei, Y. Feng, J. Ma, Co-doped graphene edge for enhanced N2-to-NH3 conversion, Journal of Energy Chemistry, 48 (2020) 322-327.

[66] G. Henkelman, A. Arnaldsson, H. Jónsson, A fast and robust algorithm for Bader decomposition of charge density, Comput. Mater. Sci., 36 (2006) 354-360.

[67] W. Chen, J. Pei, C.T. He, J. Wan, H. Ren, Y. Zhu, Y. Wang, J. Dong, S. Tian, W.C. Cheong, Rational design of single molybdenum atoms anchored on N‐doped carbon for effective hydrogen evolution reaction, Angew. Chem., 56 (2017) 16086-16090.

[68] G. Qing, R. Ghazfar, S.T. Jackowski, F. Habibzadeh, M.M. Ashtiani, C.-P. Chen, M.R. Smith III, T.W. Hamann, Recent advances and challenges of electrocatalytic N2 reduction to ammonia, Chem. Rev., 120 (2020) 5437-5516.

[69] J. Zhao, Z. Chen, Single Mo atom supported on defective boron nitride monolayer as an efficient electrocatalyst for nitrogen fixation: a computational study, Journal of the American Chemical Society, 139 (2017) 12480-12487.

[70] J. Pérez-Ramírez, N. López, Strategies to break linear scaling relationships, Nature Catalysis, 2 (2019) 971-976.

[71] Z. Seh, J. Kibsgaard, C. Dickens, I. Chorkendorff, J. Nørskov, T. Jaramillo, Combining theory and experiment in electrocatalysis: insights into materials design. Science 355: eaad4998, in, 2017.

[72] D. Bao, Q. Zhang, F.L. Meng, H.X. Zhong, M.M. Shi, Y. Zhang, J.M. Yan, Q. Jiang, X.B. Zhang, Electrochemical reduction of N2 under ambient conditions for artificial N2 fixation and renewable energy storage using N2/NH3 cycle, Adv. Mater., 29 (2017) 1604799.

[73] C. Ling, Y. Ouyang, Q. Li, X. Bai, X. Mao, A. Du, J. Wang, A general two‐step strategy–based high‐throughput screening of single atom catalysts for nitrogen fixation, Small Methods, 3 (2019) 1800376.

[74] I. Katsounaros, M.C. Figueiredo, X. Chen, F. Calle-Vallejo, M.T. Koper, Structure-and coverage-sensitive mechanism of NO reduction on platinum electrodes, ACS Catal., 7 (2017) 4660-4667.

[75] X. Guo, S. Lin, J. Gu, S. Zhang, Z. Chen, S. Huang, Establishing a theoretical landscape for identifying basal plane active 2D metal borides (MBenes) toward nitrogen electroreduction, Adv.

Funct. Mater., 31 (2021) 2008056.

[76] Z.W. Seh, J. Kibsgaard, C.F. Dickens, I. Chorkendorff, J.K. Nørskov, T.F. Jaramillo, Combining theory and experiment in electrocatalysis: Insights into materials design, Science, 355 (2017).

[77] Z. Chen, J. Zhao, C.R. Cabrera, Z. Chen, Computational screening of efficient single‑atom catalysts based on graphitic carbon nitride (g‑C3N4) for nitrogen electroreduction, Small Methods, 3 (2019) 1800368.

[78] A. Singh, B. Rohr, J. Schwalbe, M. Cargnello, K. Chan, T. Jaramillo, 464 Chorkendorff, I.; Nørskov, JK, Electrochemical Ammonia Synthesis—The Selectivity Challenge. ACS 465, Catalysis, 7 (2017) 706-709.

[79] M. Chaplin, The water molecule, liquid water, hydrogen bonds and water networks, Singapore: Pan Stanford Publishing Pte. Ltd, 2011.

[80] W. Zhao, L. Chen, W. Zhang, J. Yang, Single Mo1(W1, Re1) atoms anchored in pyrrolic-N3 doped graphene as efficient electrocatalysts for the nitrogen reduction reaction, J. Mater. Chem. A, 9 (2021) 6547-6554.